FIRST RESULTS FROM THE CHARA ARRAY. VII. LONG-BASELINE INTERFEROMETRIC MEASUREMENTS OF VEGA CONSISTENT WITH A POLE-ON, RAPIDLY ROTATING STAR

J. P. AUFDENBERG,[1,2] A. MÉRAND,[3] V. COUDÉ DU FORESTO,[3] O. ABSIL,[4] E. DI FOLCO,[3] P. KERVELLA,[3] S. T. RIDGWAY,[2,3] D. H. BERGER,[5,6] T. A. TEN BRUMMELAAR,[6] H. A. MCALISTER,[7] J. STURMANN,[6] L. STURMANN,[6] AND N. H. TURNER[6]

ABSTRACT

We have obtained high-precision interferometric measurements of Vega with the CHARA Array and FLUOR beam combiner in the K' band at projected baselines between 103 and 273 m. The measured visibility amplitudes beyond the first lobe are significantly weaker than expected for a slowly rotating star characterized by a single effective temperature and surface gravity. Our measurements, when compared to synthetic visibilities and synthetic spectrophotometry from a Roche–von Zeipel gravity-darkened model atmosphere, provide strong evidence for the model of Vega as a rapidly rotating star viewed very nearly pole-on. Our best-fitting model indicates that Vega is rotating at ~91% of its angular break-up rate with an equatorial velocity of 275 km s^{-1}. Together with the measured $v \sin i$, this velocity yields an inclination for the rotation axis of 5°. For this model the pole-to-equator effective temperature difference is ~2250 K, a value much larger than previously derived from spectral line analyses. A polar effective temperature of 10,150 K is derived from a fit to ultraviolet and optical spectrophotometry. The synthetic and observed spectral energy distributions are in reasonable agreement longward of 140 nm, where they agree to 5% or better. Shortward of 140 nm, the model is up to 10 times brighter than observed. The model has a luminosity of ~37 $L_\odot$, a value 35% lower than Vega's apparent luminosity based on its bolometric flux and parallax, assuming a slowly rotating star. Our model predicts the spectral energy distribution of Vega as viewed from its equatorial plane, and it may be employed in radiative models for the surrounding debris disk.

Subject headings: methods: numerical — stars: atmospheres — stars: fundamental parameters (radii, temperature) — stars: individual (Vega) — stars: rotation — techniques: interferometric

Online material: machine-readable table

1. INTRODUCTION

The bright star Vega (α Lyr, HR 7001, HD 172167, A0 V) has been a photometric standard for nearly 150 years. Hearnshaw (1996) describes Ludwig Seidel's visual comparative photometer measurements, beginning 1857, of 208 stars reduced to Vega as the primary standard. Today precise absolute spectrophotometric observations of Vega are available from the far-ultraviolet to the infrared (Bohlin & Gilliland 2004). The first signs that Vega may be anomalously luminous appeared in the 1960s after the calibration of the Hγ equivalent width to absolute visual magnitude [W(Hγ)-M_V] relationship (Petrie 1964). Millward & Walker (1985) confirmed Petrie's findings using better spectra and showed that Vega's M_V is 0.5 mag brighter than the mean A0 V star based on nearby star clusters. Petrie (1964) suggested the anomalous luminosity may indicate that Vega is a binary; however, the intensity interferometer measurements by Hanbury Brown et al. (1967) found no evidence for a close, bright companion, a result later confirmed by speckle observations (McAlister 1985). A faint

companion cannot be ruled out (Absil et al. 2006), although the presence of such a companion would not solve the luminosity discrepancy. Hanbury Brown et al. (1967) also noted on the basis of their angular diameter measurements that Vega's radius is 70% larger than that of Sirius. Recent precise interferometric measurements show Vega's radius ($R = 2.73 \pm 0.01\ R_\odot$; Ciardi et al. 2001) to be 60% larger than that of Sirius ($R = 1.711 \pm 0.013\ R_\odot$, $M = 2.12 \pm 0.06\ M_\odot$; Kervella et al. 2003), while the mass-luminosity and mass-radius relations for Sirius, $L/L_\odot = (M/M_\odot)^{4.3 \pm 0.2}$ and $R/R_\odot = (M/M_\odot)^{0.715 \pm 0.035}$, yield a radius for Vega only ~12% larger.

Since the work of von Zeipel (1924a, 1924b), it has been expected that in order for rapidly rotating stars to achieve both hydrostatic and radiative equilibrium, these stars' surfaces will exhibit gravity darkening, a decrease in effective temperature from the pole to the equator. In the 1960s and 1970s considerable effort (see, e.g., Collins 1963, 1966; Hardorp & Strittmatter 1968; Maeder & Peytremann 1970; Collins & Sonneborn 1977) was put into the development of models for the accurate prediction of colors and spectra from the photospheres of rapidly rotating stars. These early models showed that in the special case in which one views these stars pole-on, they will appear more luminous than nonrotating stars, yet have very nearly the same colors and spectrum. The connection between Vega's anomalous properties and the predictions of rapidly rotating model atmospheres was made by Gray (1985, 1988), who noted that Vega must be nearly pole-on and rotating at 90% of its angular breakup rate to account for its excessive apparent luminosity. Gray (1988) also noted that Vega's apparent luminosity is inconsistent with its measured Strömgren color indices, which match those of a dwarf, while the apparent luminosity suggests an evolved subgiant.

[1] Michelson Postdoctoral Fellow.
[2] National Optical Astronomy Observatory, 950 North Cherry Avenue, Tucson, AZ 85719.
[3] LESIA, UMR 8109, Observatoire de Paris-Meudon, 5 place Jules Janssen, 92195 Meudon Cedex, France.
[4] Insitut d'Astrophysique et de Géophysique, University of Liège, 17 Allée du Six Août, 40000 Liège, Belgium.
[5] Department of Astronomy, University of Michigan, 917 Dennison Building, 500 Church Street, Ann Arbor, MI 48109-1042.
[6] CHARA Array, Mount Wilson Observatory, Mount Wilson, CA 91023.
[7] Center for High Angular Resolution Astronomy, Department of Physics and Astronomy, Georgia State University, P.O. Box 3969, Atlanta, GA 30302-3969.

Another anomalous aspect of Vega is the flat-bottomed appearance of many of its weak metal lines observed at high spectral resolution and very high signal-to-noise ratio (>2000; Gulliver et al. 1991). The modeling by Elste (1992) showed that such flat-bottomed or trapazoidal profiles could result from a strong center-to-limb variation in the equivalent width of a line coupled with a latitudinal temperature gradient on the surface of the star. Soon after, Gulliver et al. (1994) modeled these unusual line profiles together with Vega's spectral energy distribution (SED) and found a nearly pole-on ($i = 5°5$), rapidly rotating ($V_{eq} = 245$ km s^{-1}) model to be a good match to these data.

Since the detection in the infrared of Vega's debris disk (Aumann et al. 1984), much of the attention paid to Vega has been focused in this regard (see, e.g., Su et al. 2005). However, not only has Vega's disk been spatially resolved, but photosphere has been as well. This was done first by Hanbury Brown et al. (1967), although attempts to measure Vega's angular diameter go back to Galileo (Hughes 2001). Recent interferometric measurements of Vega show nothing significantly out of the ordinary when compared to standard models for a slowly rotating A0 V star (Hill et al. 2004; $v \sin i = 21.9 \pm 0.2$ km s^{-1}). Specifically, uniform disk fits to data obtained in the first lobe of Vega's visibility curve, from the Mark III interferometer (Mozurkewich et al. 2003) at 500 and 800 nm and from the Palomar Testbed Interferometer (PTI; Ciardi et al. 2001) in the K band, show the expected progression due to standard wavelength-dependent limb darkening: 3.00 ± 0.05 mas (500 nm), 3.15 ± 0.03 mas (800 nm), and 3.24 ± 0.01 (K band). In addition, the first lobe data in the optical from the Navy Prototype Optical Interferometer (NPOI) yield 3.11 ± 0.01 mas ($\sim$650 nm; Ohishi et al. 2004), consistent with this picture. Ciardi et al. (2001) note small residuals in their angular diameter fits that may be due to Vega's disk.

Triple amplitude data from NPOI in May 2001 (Ohishi et al. 2004) sample the second lobe of Vega's visibility curve, where a gravity-darkening signature should be unambiguous. However, these data show the signature of limb darkening expected for a nonrotating star, as predicted by ATLAS9 limb-darkening models (van Hamme 1993). Most recently, a preliminary analysis of second-lobe NPOI data from 2003 October (Peterson et al. 2004) indicate that Vega is indeed strongly gravity darkened, a result inconsistent with Ohishi et al. (2004). Peterson et al. (2006) note that the NPOI Vega data are difficult to analyze due to detector nonlinearities for such a bright star. Peterson et al. (2006) do see a strong interferometric signal for gravity darkening from the rapid rotator Altair with an angular break-up rate 90% of critical. Since a similar rotation rate is expected for Vega on the basis of its apparently high luminosity (Gray 1988; Gulliver et al. 1994), a strong gravity darkening is expected for Vega as well.

There is clearly a need for additional high spatial resolution observations of Vega's photosphere to confirm the hypothesis of Gray (1988), confirm the 2003 NPOI observations, and test the theory of von Zeipel. We have employed the long baselines of the Center for High Angular Resolution Astronomy (CHARA) Array (ten Brummelaar et al. 2005) on Mount Wilson, together with the capabilties of the spatially filtered Fiber Linked Unit for Optical Recombination (FLUOR; Coudé du Foresto et al. 2003), as a means to probe the second lobe of Vega's visibility curve at high precision and accuracy in the K band. Our Vega campaign, part of the commissioning science (McAlister et al. 2005; Mérand et al. 2005b; van Belle et al. 2006) for the CHARA Array, obtained visibility data on baselines between 103 and 273 m that clearly show the signature of a strongly gravity darkened, pole-on,

rapidly rotating star. In this paper we present these data and a detailed modeling effort to fit both our inteferometric data and the archival data of Vega's spectral energy distribution.

We introduce our observations in § 2. Sections 3, 4, and 5 describe the construction and fitting of one- and two-dimensional synthetic brightness distributions to our interferometic data and archival spectrophotometry. A discussion of our results follows in § 6. We conclude with a summary in § 7.

2. OBSERVATIONS

Our interferometric measurements were obtained using the CHARA Array in the infrared K' band (1.94–2.34 μm) with FLUOR. Our observations were obtained during six nights in the late spring of 2005 using four telescope pairs, E2-W2, S1-W2, E2-W1, and S1-E2 with maximum baselines of 156, 211, 251, and 279 m, respectively. The FLUOR Data Reduction Software (Kervella et al. 2004; Coudé du Foresto et al. 1997) was used to extract the squared modulus of the coherence factor between the two independent telescope aperatures. We obtained 25 calibrated observations of Vega, which are summarized in Table 1. The (u, v)-plane sampling is shown in Figure 1.

The calibrator stars were chosen from the catalog of Mérand et al. (2005a). The CHARA Array's tip-tilt adaptive optics system operates at visual wavelengths. Vega is sufficiently bright that it was necessary to reduce the gain on the tip-tilt detector system while observing Vega and return the gain to the nominal setting for the fainter calibrator stars. Calibrators chosen for this work are all K giants: HD 159501 (K1 III), HD 165683 (K0 III), HD 173780 (K3 III), HD 176567 (K2 III), and HD 162211 (K2 III). The spectral type difference between the calibrators and Vega does not significantly influence the final squared visibility estimate. The interferometric transfer function of CHARA/FLUOR was estimated by observing a calibration star before and after each Vega data point. In some cases a different calibrator was used on either side of the Vega data point (see Table 1). The inteferometric efficiency of CHARA/FLUOR was consistent between all calibrators and stable over each night at $\sim$85%.

3. ONE-DIMENSIONAL MODEL FITS

Under the initial assumption that Vega's projected photospheric disk is circularly symmetric in both shape and intensity, we have fit three models to the CHARA/FLUOR data set: (1) a uniform disk, where the intensity, assumed to be Planckian [$I(\lambda) = B(T_{eff} = 9550$ K, $\lambda)$], is independent of μ, the cosine of the angle between the line-of-sight and the surface normal; (2) an analytic limb-darkening law, $I(\mu, \lambda) = B(T_{eff} = 9550$ K, $\lambda)\mu^{\alpha}$; and (3) a PHOENIX (Hauschildt et al. 1999) model radiation field with stellar parameters [$T_{eff} = 9550$ K, $\log(g) = 3.95$] consistent with the slowly rotating model that Bohlin & Gilliland (2004) show to be a good match to Vega's observed SED. The computation of the synthetic squared visibilities from these models takes into account the bandwidth smearing introduced by the nonmonochromatic FLUOR transmission (see § 4.2.1 below).

Figure 2 shows the synthetic squared visibilities from the three models in comparison with the CHARA/FLUOR data. The uniform disk angular diameter we derive ($\theta_{UD} = 3.209 \pm 0.003$ mas) is not consistent with Ciardi et al. (2001; $\theta_{UD} = 3.24 \pm 0.01$ mas). We find this is most likely because we do not assume a flat spectrum across the K'-band filter. Regardless, this uniform disk model is poor fit ($\chi^2_{\nu} = 38$) because it neglects limb darkening. The limb darkening expected for a slowly rotating star should be well predicted by the PHOENIX model, but this model is also a poor fit ($\chi^2_{\nu} = 20$, $\theta_{LD} = 3.259 \pm 0.002$ mas). The second lobe

TABLE 1
CHARA/FLUOR K'-Band Vega Measurements

No.	Julian Date	Telescope Pair	u (m)	v (m)	Projected Baseline (m)	Position Angle (deg)	V^2 ($\times 100$)	$\sigma V^2_{\text{total}}$ ($\times 100$)	Calibration Star(s) HD Number
1	2,453,511.261	E2-W2	−98.941	23.114	101.606	−76.85	21.1531	0.8846	176527
2	2,453,511.313	E2-W2	−127.859	−0.092	127.859	89.95	6.2229	0.2019	176527, 173780
3	2,453,511.347	E2-W2	−139.876	−18.250	141.062	82.56	2.6256	0.0742	173780
4	2,453,511.374	E2-W2	−144.773	−33.322	148.558	77.03	1.3567	0.0417	173780
5	2,453,512.266	E2-W2	−103.834	20.146	105.770	−79.02	18.2301	0.1976	159501
6	2,453,512.269	E2-W2	−106.062	18.698	107.698	−80.00	16.7627	0.1710	159501
7	2,453,512.277	E2-W2	−110.513	15.601	111.609	−81.96	14.4223	0.1493	159501
8	2,453,512.284	E2-W2	−114.716	12.396	115.384	−83.83	12.2229	0.1336	159501
9	2,453,512.291	E2-W2	−118.435	9.291	118.799	−85.51	10.3873	0.1168	159501
10	2,453,512.345	E2-W2	−140.179	−18.907	141.448	82.31	2.6399	0.0741	173780
11	2,453,512.349	E2-W2	−141.068	−20.951	142.615	81.55	2.3968	0.0676	173780
12	2,453,512.356	E2-W2	−142.577	−24.954	144.744	80.07	2.0041	0.0591	173780
13	2,453,516.258	E2-W1	−141.950	88.392	167.221	−58.08	0.1040	0.0059	159501
14	2,453,516.343	E2-W1	−224.986	25.325	226.407	−83.57	1.2148	0.0521	159501, 165683
15	2,453,517.248	E2-W1	−132.597	92.319	161.569	−55.15	0.2426	0.0194	159501, 173780
16	2,453,517.288	E2-W1	−180.244	67.502	192.469	−69.46	0.5913	0.0314	173780
17	2,453,517.342	E2-W1	−225.788	24.193	227.080	−83.88	1.1066	0.0670	173780
18	2,453,519.225	E2-S1	−169.006	−165.745	236.716	45.55	1.1361	0.0414	159501
19	2,453,519.252	E2-S1	−168.472	−183.482	249.095	42.55	0.9120	0.0344	159501
20	2,453,519.285	E2-S1	−161.265	−205.029	260.851	38.18	0.6047	0.0259	159501
21	2,453,519.316	E2-S1	−147.913	−224.292	268.673	33.40	0.5079	0.0238	159501
22	2,453,522.270	E2-S1	−163.306	−200.735	258.773	39.13	0.5911	0.0427	159501
23	2,453,522.306	E2-S1	−148.868	−223.205	268.295	33.70	0.4518	0.0241	159501
24	2,453,522.336	E2-S1	−131.105	−239.777	273.279	28.67	0.3788	0.0199	159501
25	2,453,538.206	W2-S1	56.624	202.948	210.699	15.59	0.9303	0.0682	162211

data indicate that Vega is significantly more limb darkened compared to this model. The nonphysical $I(\mu) = \mu^\alpha$ model yields a much better fit ($\chi^2_\nu = 1.5$) and a significantly larger angular diameter $\theta_{\text{LD}} = 3.345 \pm 0.006$ ($\alpha = 0.341 \pm 0.013$), which suggests the limb-darkening correction in the K' band is ~2.5 times larger (4.2% vs. 1.6%) than expected for a slowly rotating Vega.

Absil et al. (2006) report that a small fraction ($f = 1.29\% \pm 0.16\%$) of Vega's K'-band flux comes from an extended structure,
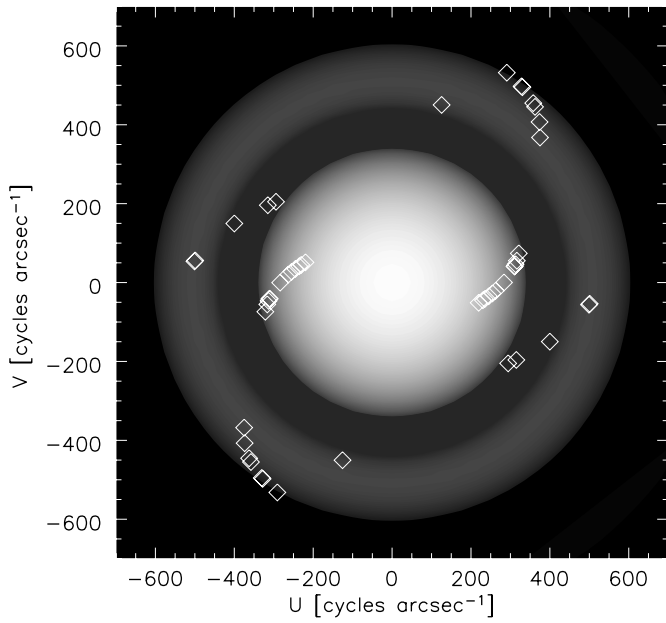

Fig. 1.—Sampling of the (u, v)-plane for the CHARA/FLUOR Vega data set. The diamonds represent the monochromatic sampling at 2.0 μm within the K' band. In the K' band, the CHARA baselines E2-W2, E2-W1, E2-S1, and W2-S1 sample the lower first lobe, first null, and second lobe of Vega's visibility curve. Two-telescope observations have a 180° ambiguity in the position angle, therefore we plot two coordinates, (u, v) and $(-u, -v)$, for each of the 25 data points. These (u, v) points overlay a model for Vega's two-dimensional monochromatic Fourier appearance. This squared visibility model is a Fast Fourier Transform (displayed with a logarithmic stretch) of a synthetic intensity map of Vega in the plane of the sky (see Fig. 3).
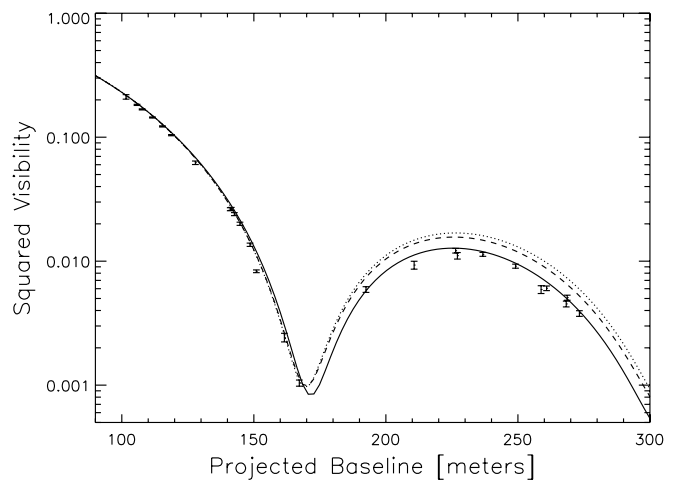

Fig. 2.—Best-fit one-dimensional, symmetric models in comparison with the CHARA/FLUOR data set. The dotted line is a bandwidth-smeared uniform disk ($\chi^2_\nu = 38$, $\theta_{\text{UD}} = 3.209 \pm 0.003$ mas) The dashed line is a bandwidth-smeared PHOENIX model atmosphere with parameters consistent with a slowly rotating Vega [$T_{\text{eff}} = 9550$ K, $\log(g) = 3.95$, $\chi^2_\nu = 20$, $\theta_{\text{LD}} = 3.259 \pm 0.002$ mas], and the solid line a bandwidth-smeared analytic limb-darkening model, $I(\mu) = \mu^\alpha$ ($\chi^2_\nu = 1.5$, $\theta_{\text{LD}} = 3.345 \pm 0.006$ mas, $\alpha = 0.341 \pm 0.013$). If extended emission in the K' band is present at the 1.3% level in the Vega system, these best angular diameters are systematically high by ~3 σ (see text).

most likely Vega's debris disk. In order to gauge the significance of this extra flux on the photospheric parameters derived above, the synthetic squared visibilities are reduced by an amount equal to the square of fraction of light coming from the debris disk. At long baselines, the visibility of the debris disk is essentially zero such that

$$V_{\text{obs}}^2 = \left[(1-f)V_{\text{photosphere}} + f V_{\text{disk}}\right]^2 \quad (1)$$
$$\approx 0.974 V_{\text{photosphere}}^2.$$

The revised fits to $V_{\text{photosphere}}^2$ are $\theta_{\text{UD}} = 3.198 \pm 0.003$ ($\chi_\nu^2 = 38$) for the uniform disk, $\theta_{\text{LD}} = 3.247 \pm 0.002$ ($\chi_\nu^2 = 19$) for the PHOENIX model, and $\theta_{\text{LD}} = 3.329 \pm 0.006$ ($\alpha = 0.328 \pm 0.013$, $\chi_\nu^2 = 1.4$) for the $I(\mu) = \mu^\alpha$ model. The effect of removing the extended emission is to reduce the best-fit angular diameter for all three models by $\sim 3\,\sigma$; the correction for extended emission is therefore significant.

4. TWO-DIMENSIONAL MODEL CONSTRUCTION

In order to physically interpret the strong limb darkening we find for Vega, we have adapted a computer program written by S. Cranmer (2002, private communication) from Cranmer & Owocki (1995) that computes the effective temperature and surface gravity on the surface of a rotationally distorted star, specifically a star with an infinitely concentrated central mass under uniform angular rotation, a Roche–von Zeipel model. This azimuthally symmetric model is parameterized as a function of the colatitude given the mass, polar radius, luminosity, and fraction of the angular break-up rate.

Each two-dimensional intensity map is characterized by five variables: θ_{equ}, the angular size of the equator, equivalent to the angular size as viewed exactly pole-on; $\omega = \Omega/\Omega_{\text{crit}}$, the fraction of the critical angular break-up rate; $T_{\text{eff}}^{\text{pole}}$, the effective temperature at the pole; $\log(g)_{\text{pole}}$, the effective surface gravity at the pole; and ψ, the position angle of the pole on the sky measured east from north.

Given these input parameters, along with the measured trigonometric parallax $\pi_{\text{hip}} = 128.93 \pm 0.55$ mas (Perryman et al. 1997), and the observed projected rotation velocity, $v \sin i = 21.9 \pm 0.2$ km s^{-1} (Hill et al. 2004), the parameterization of the intensity maps begins with

$$R_{\text{equ}} = 107.48 \frac{\theta_{\text{equ}}}{\pi_{\text{hip}}}, \quad (2)$$

with the equatorial radius in solar units and both θ_{equ} and π_{hip} in milliarcseconds. It follows from a Roche model (Cranmer & Owocki 1995; eq. [26]) that the corresponding polar radius is

$$R_{\text{pole}} = \frac{\omega R_{\text{equ}}}{3 \cos\left[\frac{\pi + \cos^{-1}(\omega)}{3}\right]}$$

and the stellar mass is

$$M = \frac{g_{\text{pole}} R_{\text{pole}}^2}{G}, \quad (4)$$

where G is the universal gravitational constant. The luminosity is then

$$L = \frac{\sigma \Sigma \left(T_{\text{eff}}^{\text{pole}}\right)^4}{g_{\text{pole}}}, \quad (5)$$

where σ is the Stefan-Boltzman constant and Σ is the surface-weighted gravity (Cranmer & Owocki 1995; eqs. [31] and [32]), expressed as a power series expansion in ω,

$$\Sigma \approx 4\pi GM \big(1.0 - 0.19696\omega^2 - 0.094292\omega^4 + 0.33812\omega^6$$
$$- 1.30660\omega^8 + 1.8286\omega^{10} - 0.92714\omega^{12}\big). \quad (6)$$

The ratio of the luminosity to Σ provides the proportional factor between the effective temperature and gravity for von Zeipel's radiative law for all colatitudes ϑ:

$$T_{\text{eff}}(\vartheta) = \left[\frac{L}{\sigma\Sigma} g(\vartheta)\right]^\beta = T_{\text{eff}}^{\text{pole}} \left[\frac{g(\vartheta)}{g_{\text{pole}}}\right]^\beta, \quad (7)$$

where the gravity darkening parameter, β, takes the value 0.25 in the purely radiative case (no convection). The effective temperature difference between the pole and equator, ΔT_{eff}, may be expressed in terms of $T_{\text{eff}}^{\text{pole}}$ and ω:

$$\Delta T_{\text{eff}} = T_{\text{eff}}^{\text{pole}} - T_{\text{eff}}^{\text{equ}} = T_{\text{eff}}^{\text{pole}} \left[1 - \left(\frac{\omega^2}{\eta^2} - \frac{8}{27}\eta\omega\right)^\beta\right], \quad (8)$$

where

$$\eta = 3 \cos\left[\frac{\pi + \cos^{-1}(\omega)}{3}\right].$$

The effective gravity as a function of ϑ is given by

$$g(\vartheta) = \left[g_r(\vartheta)^2 + g_\vartheta(\vartheta)^2\right]^{1/2}, \quad (9)$$

$$g_r(\vartheta) = \frac{-GM}{R(\vartheta)^2} + R(\vartheta)(\Omega \sin \vartheta)^2, \quad (10)$$

$$g_\vartheta(\vartheta) = R(\vartheta)\Omega^2 \sin \vartheta \cos \vartheta, \quad (11)$$

where g_r and g_ϑ are the radial and colatitudinal components of the gravity field. The colatitudinal dependence of the radius is given by

$$R(\vartheta) = 3 \frac{R_{\text{pole}}}{\omega \sin \vartheta} \cos\left[\frac{\pi + \cos^{-1}(\omega \sin \vartheta)}{3}\right] \quad (\omega > 0) \quad (12)$$

and angular rotation rate is related to the critical angular rotation rate[8] by

$$\Omega = \omega \Omega_{\text{crit}} = \omega \left(\frac{8}{27} \frac{GM}{R_{\text{pole}}^3}\right)^{1/2}. \quad (13)$$

At the critical rate ($\omega = 1$), $R_{\text{equ}} = 1.5 R_{\text{pole}}$. The inclination follows from

$$i = \sin^{-1}\left(\frac{v \sin i}{V_{\text{equ}}}\right), \quad (14)$$

[8] There is a typographical error in eq. (5) of Collins (1963), which is not in the paper's erratum (Collins 1964): $\omega_c^2 = GM/R_e$ should be $\omega_c^2 = GM/R_e^3$, where ω_c the critical angular rate and R_e is the equatorial radius at the critical rate.

where the equatorial velocity is

$$V_{\mathrm{equ}} = R_{\mathrm{equ}}\Omega. \tag{15}$$

4.1. Building the Intensity Maps

For each wavelength λ (185 total wavelength points: 1.9–2.4 μm in 0.005 μm steps, with additional points for H I and He I profiles calculated in non-LTE), an intensity map is computed as follows: $T_{\mathrm{eff}}(\vartheta)$ and $\log((g)\vartheta)$ are evaluated at 90 ϑ points from $0°$ to $90° + i$. At each ϑ there are 1024 longitude φ points from $0°$ to $360°$ to finely sample the perimeter of the nearly pole-on view. For Vega's nearly pole-on orientation, the relatively high resolution in φ reduces numerical aliasing when the brightness map is later interpolated onto a uniformly gridded rectangular array as described below.

Each set of spherical coordinates $[R(\vartheta), \vartheta, \varphi]$ is first transformed to rectangular (x, y, z) coordinates with the Interactive Data Language (IDL) routine POLEREC3D.[9] Next, the z-axis of the coordinate system is rotated away from the observer by an angle equal to the inclination i (using the IDL routine ROT_3D) and then the (x, y)-plane is rotated by an angle equal to ψ, the position angle (east of north) of the pole on the sky (using the IDL routine ROTATE_XY).

At each point in the map, the cosine of the angle between the observer's line of sight and the local surface normal is

$$\mu(x, y) = \mu(\vartheta, \varphi, i)$$
$$= \frac{1}{g(\vartheta)}\left[- g_r(\vartheta)(\sin\vartheta\sin i\cos\varphi + \cos\vartheta\cos i) \right.$$
$$\left. - g_\vartheta(\vartheta)(\sin i\cos\varphi\cos\vartheta - \sin\vartheta\cos i) \right]. \tag{16}$$

The intensity at each point (x, y) is interpolated from a grid of 170 spherical, hydrostatic PHOENIX (vers. 13.11.00B) stellar atmosphere models (Hauschildt et al. 1999) spanning 6500 to 10,500 K in T_{eff} and 3.25 to 4.15 in $\log(g)$:

$$T_j = 6500 + 250j \text{ K}, \quad j = \{0, 1, \ldots, 16\},$$
$$\log(g_l) = 3.25 + 0.1l, \quad l = \{0, 1, \ldots, 9\}.$$

Four radiation fields, $I(\lambda, \mu)$ evaluated at 64 angles by PHOENIX, are selected from the model grid to bracket the local effective temperature and gravity values on the grid square,

$$T_j < T_{\mathrm{eff}}(\vartheta) < T_{j+1},$$
$$g_l < g(\vartheta) < g_{l+1}.$$

The intensity vectors $I_\lambda(\mu)$ are linearly interpolated (in the log) at $\mu(x, y)$ around the grid square,

$$I_\lambda^{00} = I_\lambda(T_j, g_l, \mu(x, y)),$$
$$I_\lambda^{10} = I_\lambda(T_{j+1}, g_l, \mu(x, y)),$$
$$I_\lambda^{11} = I_\lambda(T_{j+1}, g_{l+1}, \mu(x, y)),$$
$$I_\lambda^{01} = I_\lambda(T_j, g_{l+1}, \mu(x, y)).$$

[9] The coordinate transformation routines used here are from the JHU/APL/S1R IDL library of the Space Oceanography Group of the Applied Physics Laboratory of Johns Hopkins University.

Next, the intensity is bilinearly interpolated at the local T_{eff} and $\log(g)$ for each (x, y) position in the map:

$$I_\lambda(x, y) = I_\lambda[T_{\mathrm{eff}}(x, y), g(x, y), \mu(x, y)]$$
$$= (1 - a)(1 - b)I_\lambda^{00} + a(1 - b)I_\lambda^{10}$$
$$+ abI_\lambda^{11} + (1 - a)bI_\lambda^{01} \tag{17}$$

where

$$a = \left[T_{\mathrm{eff}}(x, y) - T_j \right] / \left(T_{j+1} - T_j \right),$$
$$b = \left[g(x, y) - g_l \right] (g_{l+1} - g_l).$$

Finally, a Delaunay triangulation is computed (using the IDL routine TRIGRID) to regrid the intensity map $I_\lambda(x, y)$, originally gridded in ϑ and φ, onto a regular 512×512 grid of points in x and y. The coordinates x and y have the units of milliarcseconds and correspond to offsets in right ascension and declination on the sky $(\Delta\alpha, \Delta\delta)$ relative to the origin, the subsolar point.

4.2. Synthetic Squared Visibility Computation

Due to the lack of symmetry in the synthetic intensity maps, we evaluate a set of discrete two-dimensional Fourier transforms in order to generate a set of synthetic squared visibilities comparable to the CHARA/FLUOR observations. The first step is to compute the discrete Fourier transform for each wavelength at each of the spatial frequency coordinates (u, v) corresponding to the projected baseline and orientation of each data point (see Table 1). The mean (u, v) coordinates for each data point, in units of meters, are converted to the corresponding spatial frequency coordinates (u_k, v_k) in units of cycles per arcsecond for each wavelength λ_k. The Fourier transform

$$V_\lambda^2(u, v) = \left[\int_{-\infty}^{\infty} \int_{-\infty}^{\infty} S_\lambda I_\lambda(x, y) e^{i2\pi(ux+vy)}\, dx\, dy \right]^2 \tag{18}$$

is approximated by the integration rule of Gaussian quadrature (e.g., Stroud & Secrest 1966; Press et al. 1992):

$$V_k^2(u_k, v_k) \approx \left\{ \sum_{i=1}^{N} A_i \sum_{j=1}^{N} A_j S_k I_k(x_i, y_j) \cos\left[2\pi(u_k x_i + v_k y_j) \right] \right\}^2$$
$$+ \left\{ \sum_{i=1}^{N} A_i \sum_{j=1}^{N} A_j S_k I_k(x_i, y_j) \sin\left[2\pi(u_k x_i + v_k y_j) \right] \right\}^2, \tag{19}$$

where S_k is the wavelength discretized value of the instrument sensitivity curve S_λ, and A_i, A_j and x_i, y_j are the weights and nodes of the quadrature, respectively. For our square grid, the x- and y-coordinate nodes and weights are identical. The two-dimensional Gaussian quadrature is performed with a version of the IDL routine INT_2D modified to use an arbitrarily high number of nodes. The intensity at wavelength k, $I_k(x, y)$, is interpolated at (x_i, y_j) from the regular 512×512 spacing to the quadrature node points using the IDL routine INTERPOLATE which uses a cubic convolution interpolation method employing 16 neighboring points. The synthetic squared visibility is normalized to unity at zero spatial frequency by

$$V_k^2(0, 0) \approx \left[\sum_{i=1}^{N} A_i \sum_{j=1}^{N} A_j S_k I_k(x_i, y_j) \right]^2. \tag{20}$$

We find $N = 512$ provides the degree of numerical accuracy sufficient in the case of a two-dimensional uniform disk (right circular cylinder) to yield V^2 values in agreement with the analytic result,

$$V_k^2(u_k,\ v_k) = \left[2J_1\left(\pi\theta\sqrt{u_k^2 + v_k^2}\right) \Big/ \left(\pi\theta\sqrt{u_k^2 + v_k^2}\right) \right]^2, \quad (21)$$

where J_1 is the first order Bessel function of the first kind, θ is the angular diameter of the uniform disk, and B is the projected baseline, to better than 1% for $V^2 > 10^{-3}$. We use the IDL function BESELJ for our J_1 computations. For $V^2 \lesssim 10^{-4}$, near the monochromatic first and second zeros, the numerical accuracy of the quadrature deteriorates to 10% or worse. The bandwidth-smeared V^2 minimum is at $\sim 10^{-3}$, so we find this quadrature method yields squared visibilities which are sufficiently accurate for our task, however observations with an even larger dynamic range (Perrin & Ridgway 2005) will require more accurate methods.

To test the two-dimensional Gaussian quadrature method in the case where no analytic solution is available, we computed the two-dimensional fast Fourier transform (IDL routine FFT) of a brightness map (see Fig. 3). First, we compared the results of the two-dimensional FFT to the analytic uniform disk (eq. [21]). To reduce aliasing we find it necessary to "zero-pad" the brightness map. With 12-to-1 zero padding (the 512×512 brightness map placed at the center of a larger 6144×6144 array of zeros), we find the two-dimensional FFT has very similar accuracy to the 512-point Gaussian quadrature: better than 1% down to $V^2 \gtrsim 10^{-3}$ inside the second null. For the brightness map shown in Figure 3, the two-dimensional FFT and Gaussian quadrature methods agree to better than 0.5% down to $V^2 \gtrsim 10^{-3}$, inside the second null. We find the computational time required to evaluate equation (19) at 25 $(u_k,\ v_k)$ points for 185 wavelengths is ~ 6 times faster than the evaluation of the 185 zero-padded two-dimensional FFTs.

4.2.1. Bandwidth Smearing

Once we have computed $V_k^2(u_k,\ v_k)$ for the 185 wavelength points, we proceed to compute the bandwidth-smeared average squared visibility $V(B,\ \lambda_0)^2$,

$$V(B,\ \lambda_0)^2 = \frac{\int_0^\infty V(B,\ \lambda)^2 \lambda^2\, d\lambda}{\int_0^\infty V(0,\ \lambda)^2 \lambda^2\, d\lambda}. \quad (22)$$

This integral is performed by the IDL routine INT_TABULATED, a five-point Newton-Cotes formula. The λ^2 term is included so that the integral is equivalent to an integral over wavenumber (frequency), where

$$\lambda_0^{-1} = \frac{\int_0^\infty \lambda^{-1} S(\lambda) F_\lambda\, d\lambda}{\int_0^\infty S(\lambda) F_\lambda\, d\lambda} \quad (23)$$

is the mean wavenumber. This simulates the data collection and fringe processing algorithm used by FLUOR. In the discretized integrand $V(B,\ \lambda_k)^2$ is equivalent to $V_k^2(u_k,\ v_k)$, where $B = 206264.8\lambda_k\left(u_k^2 + v_k^2\right)^{1/2}$, with λ_k in units of meters and u_k and v_k in units of cycles per arcsecond.

4.3. *Synthetic Spectral Energy Distribution Construction*

To construct synthetic SEDs for Vega from the Roche–von Zeipel model, 170 radiation fields were computed from the same model grid used to construct the K'-band intensity maps. The
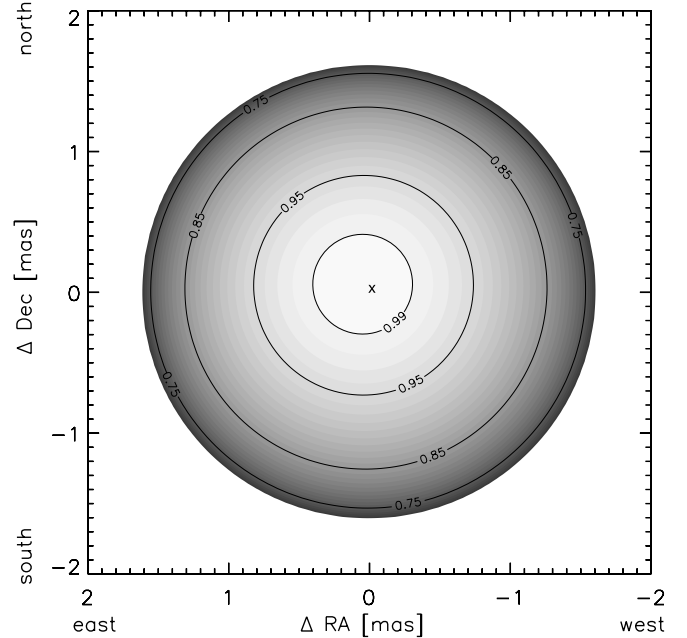

FIG. 3.—Synthetic brightness map (linear stretch) of Vega for our best-fitting parameters: $\omega = 0.91$, $\theta_{\rm equ} = 3.329$ mas, $T_{\rm eff}^{\rm pole} = 10,150$ K, $\log(g)_{\rm pole} = 4.10$. For this model, Vega's pole is inclined $5°$ toward a position angle of $40°$, with the subsolar point marked with an "x." The labeled intensity contours are relative to the maximum intensity in the map.

wavelength resolution is 0.05 nm from 100 to 400 nm, 0.2 nm from 400 nm to 3 μm, and 10 nm from 3 to 50 μm. The higher resolution in the ultraviolet is needed to sample the strong line blanketing in this spectral region. From the resulting grid of radiation fields, intensity maps are computed (see § 4.1), and the flux is computed from

$$F_\lambda = \int_0^\pi \int_0^{2\pi} -\frac{g(\vartheta)}{g_r(\vartheta)} I_\lambda(R, \vartheta, \varphi) R(\vartheta)^2 \sin\vartheta \mu(\vartheta, \varphi, i)\, d\varphi\, d\vartheta.$$

$$(24)$$

This two-dimensional integral is performed with the IDL routine INT_TABULATED_2D (vers. 1.6), which first constructs a Delaunay triangulation of points in the $(\vartheta,\ \varphi)$-plane. For each triangle in the convex hull (defined as the smallest convex polygon completely enclosing the points), the volume of the triangular cylinder formed by six points (the triangle in the plane and three points above with heights equal to the integrand) is computed and summed. For computing the flux from the intensity maps, a coarser sampling in ϑ and φ (20×40), relative to that needed for the visibility computations, is sufficient for better than 1% flux accuracy. The numerical accuracy was checked by computing the SED of a nonrotating star ($\omega = 0$) and comparing this to a single effective temperature SED from a one-dimensional atmosphere. The interpolation and integration errors result in a flux deficit of less than 0.7% at all wavelengths relative to the one-dimensional model atmosphere.

5. TWO-DIMENSIONAL MODEL FITTING

5.1. *Initial Parameter Constraints*

The computation of each intensity map, the Fourier transforms, and the bandwidth-smearing for each set of input parameters $[\theta_{\rm equ}, \omega, T_{\rm eff}^{\rm pole}, \log(g)_{\rm pole}, \psi]$ is too computationally expensive to compute synthetic squared visibilities many hundreds of times as part
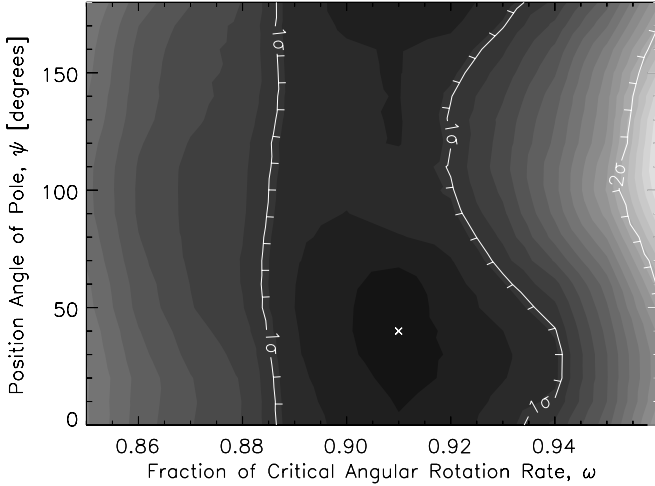
Fig. 4.—Contour plot of χ_ν^2 in the $(\omega,\ \psi)$-plane for $T_{\rm eff}^{\rm pole} = 10{,}250$ K and $\log(g)_{\rm pole} = 4.1$. The labeled contours denote the lower and upper 1σ range, and a 2σ contour, from the F test. The cross marks the best fit, $\chi_\nu^2 = 1.31$, while the brightest region has a $\chi_\nu^2 = 3.25$ (see Fig. 6).

Fig. 5.—(a) CHARA/FLUOR V^2 data (error bars) plotted as a function of projected baseline (for a range of azimuths, see Table 1) together with the best-fitting Roche–von Zeipel synthetic squared visibilities. Model parameters: $\omega = 0.91$, $\theta_{\rm equ} = 3.329$ mas, $T_{\rm eff}^{\rm pole} = 10{,}250$ K, $\log(g)_{\rm pole} = 4.10$. The best-fit $\chi_\nu^2 = 1.31$. (b) Deviations of the best-fit model from observed squared visibilities. The dotted and dashed lines indicated the 1 and 2 σ deviations.

of a gradient-search method over the vertices of a five-dimensional hypercube. Therefore, we must proceed with targeted trial searches to establish the sensitivity of χ_ν^2 to each parameter after first establishing a reasonable range of values for each parameter.

The parameter $\theta_{\rm equ}$ is a physical angular diameter related to a uniform disk fit by a scale factor depending on the degree of gravity and limb darkening, which in turn depends on the parameters ω, $\log(g)_{\rm pole}$, and $T_{\rm eff}^{\rm pole}$, in order of importance. As shown above, a limb-darkening correction of 4% is significantly larger than the $\sim$1.5% value expected for a normal A0 V star at 2 μm (Davis et al. 2000). The analytic limb-darkening model fit is sufficiently good that we take $\theta_{\rm equ} = 3.36$ mas as a starting value. This corresponds to $R_{\rm equ} = 2.77\ R_\odot$ from equation (2).

Our starting value for ω is based on the assumption that Vega's *true* luminosity should be similar to that slowly rotating A0 V stars. Vega has an apparent luminosity, assuming a single effective temperature from all viewing angles, of 57 $L_\odot$ based on its bolometric flux and the parallax. In the pole-on rapidly rotating case, we would see Vega in its brightest projection. According to Millward & Walker (1985) the mean absolute visual magnitude, M_V, is 1.0 for spectral type A0 V. With a bolometric correction of -0.3, this translates to $L = 37.7\ L_\odot$. From equations (5) and (6) we expect $\omega > 0.8$ in order to account for the luminosity discrepancy assuming a minimum polar effective temperature of 9550 K, based on the nonrotating model fits to Vega's SED (Bohlin & Gilliland 2004). The range of effective temperatures and surface gravities for the model atmosphere grid described in § 4.1 sets our upper rotation limit at $\omega \le 0.96$. For $\omega > 0.8$, $\Delta T_{\rm eff} > 1300$ K (see eq. [8]), and thus $T_{\rm eff}^{\rm pole}$ must be greater than 9550 K to compensate for the pole-to-equator temperature gradient and to reproduce the observed SED. So, given a mean apparent $T_{\rm eff}$ of 9550 K, a rough estimate of $T_{\rm eff}^{\rm pole}$ is 9550 K $+ \frac{1}{2}\Delta T_{\rm eff} = 10{,}200$ K. We therefore limit the polar effective temperature to the range 10,050 K $< T_{\rm eff}^{\rm pole} <$ 10,350 K.

The relationship between ω and the true luminosity, through equations (5), (6), and (4), is independent of the polar surface gravity; yet we can constrain $\log(g)_{\rm pole}$ by assuming Vega follows the mass-luminosity relation we derive for the slowly rotating Sirius, $L/L_\odot = (M/M_\odot)^{4.3 \pm 0.2}$. Here we assume Vega's rapid rotation has no significant effect on its interior in relation to the luminosity from nuclear reactions in its core. Assuming $L =$
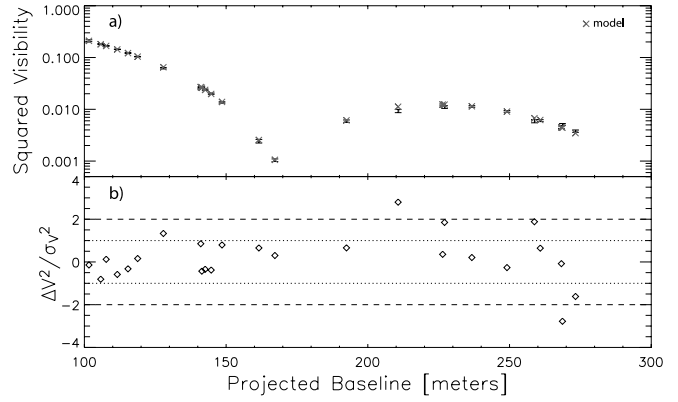
37.7 $L_\odot$ from above, the mass-luminosity relation yields $M = 2.3 \pm 0.1\ M_\odot$. As ω increases, $R_{\rm pole}$ decreases relative to $R_{\rm equ}$, therefore choosing $M = 2.2\ M_\odot$ and $\omega = 0.8$ provides a lower limit of $\log(g)_{\rm pole} = 4.0$. For lower polar gravities, Vega's mass will be significantly lower than expected based on its luminosity; nevertheless, we choose a range $\log(g)_{\rm pole}$ values from 3.6 and 4.3 in order to check the effect of the gravity on our synthetic visibilities and SEDs.

Finally, the position angle of Vega's pole, ψ, should be important if Vega's inclination is sufficiently high *and* its rotation sufficiently rapid to produce an elliptical projection of the rotationally distorted photosphere on plane of the sky. Previous measurements (Ohishi et al. 2004; Ciardi et al. 2001) find no evidence for ellipticity. Preliminary results from the NPOI three-telescope observations of Peterson et al. (2004) suggest an asymmetric brightness distribution with $\psi = 281^\circ$.

5.2. CHARA/FLUOR Data: Parameter Grid Search

For the grid search we compute the χ_ν^2 for a set of models defined by $\theta_{\rm equ}, \omega, T_{\rm eff}^{\rm pole}, \log(g)_{\rm pole}$, and ψ, adjusting $\theta_{\rm equ}$ slightly ($<$0.3%) to minimize χ_ν^2 for each model (see below). Figure 4 shows a χ_ν^2 map in the $(\omega,\ \psi)$-plane for a range of $\theta_{\rm equ}$ values with $T_{\rm eff}^{\rm pole} = 10{,}250$ K, $\log(g)_{\rm pole} = 4.1$. We find a best fit of $\chi_\nu^2 = 1.31$ for parameters $\omega = 0.91$, $\theta_{\rm equ} = 3.329$ mas, and $\psi = 40^\circ$. A direct comparison of this model with the squared visibility data is shown in Figure 5.

The F-test provides a 1 σ lower limit on ω at $\simeq$0.89. For $\omega < 0.89$, the synthetic V^2 values are generally too high across the second lobe because the model is not sufficiently darkened toward the limb. Correspondingly, the upper limits on ω are constrained because the synthetic V^2 values are generally too low across the second lobe, due to very strong darkening toward the limb for $\omega \gtrsim 0.93$. In addition, the upper limit on ω is a function of ψ because the projected stellar disk appears sufficiently more elliptical, even at low inclinations $i \simeq 5^\circ$, as the model star rotates faster. The data from the nearly orthogonal E2-W1 and E2-S1 baselines constrain models with $\omega > 0.92$ to limited range of position angles, but these data provide no constraint on ψ at lower ω-values where the star is less distorted, $R_{\rm equ}/R_{\rm pole} < 1.24$.

As ω increases so does the darkening of the limb due to the increasing larger pole-to-equator effective temperature difference. As a result, the best-fit $\theta_{\rm equ}$ value increases with ω because
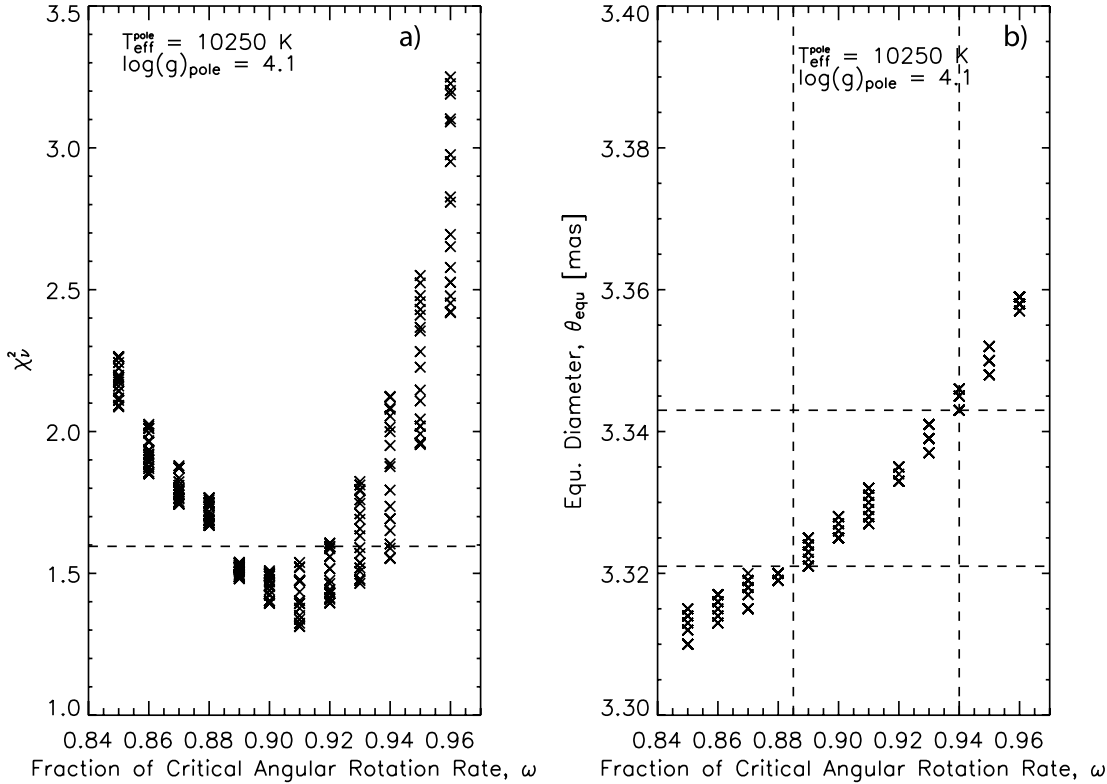
Fig. 6.—Constraints on model parameters from the CHARA/FLUOR data. (*a*) Reduced χ^2 values χ_ν^2 from the Roche–von Zeipel model fit to the squared visibility data as a function the fraction of the critical angular break-up rate, $\omega = \Omega/\Omega_{\rm crit}$, for fixed values of the polar effective temperature $T_{\rm eff}^{\rm pole}$ and polar surface gravity $\log(g)_{\rm pole}$. The dashed line denotes the 1 σ confidence region for ω from the *F* test for 24 degrees of freedom relative to the best fit at $\chi_\nu^2 = 1.31$. For each ω, χ_ν^2 values are plotted for 18 position angles ψ ($0°$ to $170°$ in $10°$ steps; see Fig. 4). (*b*) Relationship between the best-fit equatorial angular diameter $\theta_{\rm equ}$ at each ω for the range of position angles. The dashed lines provide an estimate for the 1 σ range in ω and the corresponding range in the equatorial angular diameter.

the effective "limb-darkening" correction increases. The best-fit values for $\theta_{\rm equ}$ and ω are therefore correlated. To establish this correlation, we estimated the best-fitting $\theta_{\rm equ}$ value for a given ω without recomputing the brightness map and Fourier components. While each intensity map is constructed for a fixed $\theta_{\rm equ}$ value, we can approximate the squared visibilities for models with slightly ($<0.5\%$) larger or smaller $\theta_{\rm equ}$ values as follows. A small adjustment to V^2 due to a small adjustment in $\theta_{\rm equ}$, assuming the physical model for the star is not significantly changed and the model changes relatively slowly with wavelength, is equivalent to computing V^2 at a larger (smaller) wavelength for a larger (smaller) value of $\theta_{\rm equ}$. So, for a given projected baseline, we linearly interpolate (in the log) $V_\lambda^2(u, v)$ at $\lambda = \lambda_k\left(\theta_{\rm fit}/\theta_{\rm equ}\right)$, a wavelength shift of 10 nm or less. Near the bandpass edges, the instrument transmission drops to zero, so there is no concern about interpolating outside of the wavelength grid with this scheme. The V^2 normalization, equation (20), must be scaled by the $\left(\theta_{\rm fit}/\theta_{\rm equ}\right)^2$ to compensate for the revised surface area of the star. After one iteration, setting $\theta_{\rm equ} = \theta_{\rm fit}$, recomputing the Fourier map and refitting the data, the best-fit $\theta_{\rm equ}$ value is within 0.25% of that found with the estimated model V^2 values.

Figure 6*a* shows the χ_ν^2 values from Figure 4 projected on the ω axis, with a spread of values for the 18 position angles at each ω-value. This shows again that for the range $0.89 < \omega < 0.92$ there is no constraint on the position angle of the pole. The corresponding best-fit $\theta_{\rm equ}$ values are shown in Figure 6*b*. The equatorial angular diameter is constrained to the range 3.32 mas < $\theta_{\rm equ}$ < 3.34 mas. The best fit to the CHARA/FLUOR data is insensitive to $T_{\rm eff}^{\rm pole}$. This is because $\Delta T_{\rm eff}$, which determines the overall darkening, is quite sensitive to ω, but $T_{\rm eff}^{\rm pole}$ is not (see

eq. [8]). Thus, we cannot usefully constrain $T_{\rm eff}^{\rm pole}$ or ψ from the CHARA/FLUOR data. As for the surface gravity, varying $\log(g)_{\rm pole}$ over what we consider the most probable range, 4.1 ± 0.1, does not significantly effect the χ_ν^2 minimum. Models with $\log(g)_{\rm pole}$ values from 3.9 to 4.3 all fall within 1 σ of the best fit. The best-fit $\theta_{\rm equ}$ values are essentially independent of $T_{\rm eff}^{\rm pole}$ between 9800 and 10,450 K and weakly dependent on $\log(g)_{\rm pole}$
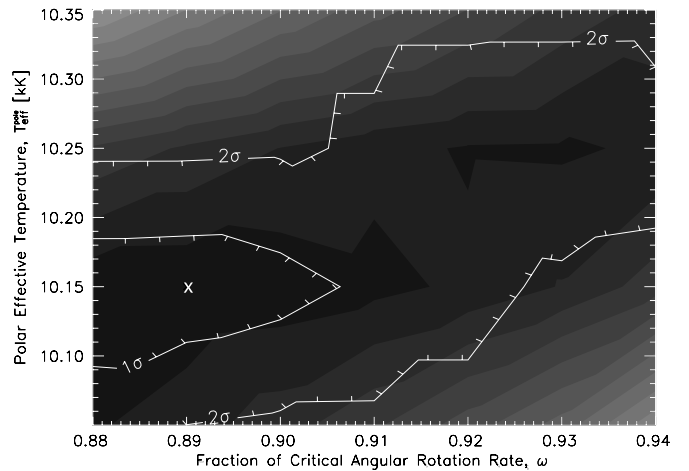

Fig. 7.—Contour plot of χ_ν^2 for the SED fits in the (ω, $T_{\rm eff}^{\rm pole}$)-plane. The ω range is limited to the 1 σ range from CHARA/FLUOR fits (see Fig. 6). The polar surface gravity is fixed at $\log(g)_{\rm pole} = 4.1$. The labeled contours denote the 1 and 2 σ regions from the *F* test. The cross marks the location of the best-fit model, $\chi_\nu^2 = 8.7$.
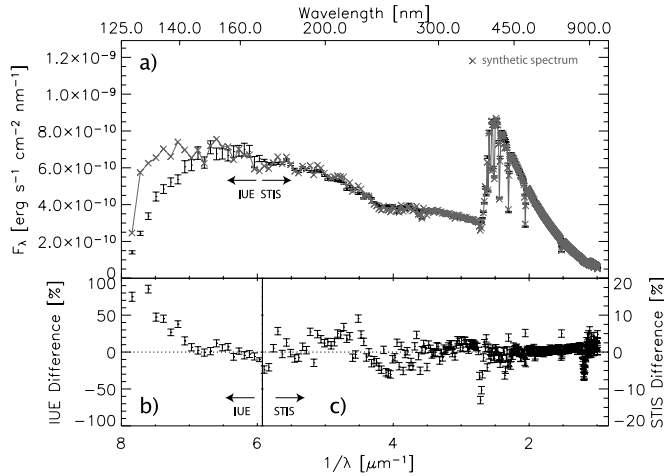
Fig. 8.—(a) Comparison between the SED of Bohlin & Gilliland (2004) and our best-fitting ($\chi_\nu^2 = 8.7$) rapidly rotating SED model for Vega: $\omega = 0.91$, $T_{\rm eff}^{\rm pole} = 10,150$ K, and $\log (g)_{\rm pole} = 4.10$. Also shown are the differences between this model and the data in (b) the region at shorter wavelengths observed by the *IUE* and (c) the region observed by the *HST* Space Telescope Imaging Spectrograph at longer wavelengths. At wavenumbers $1/\lambda < 2.38\ \mu{\rm m}^{-1}$ the "observed" SED is represented by a closely fitting Kurucz model spectrum (see Bohlin & Gilliland 2004).

between 3.8 and 4.3; all best-fit $\theta_{\rm equ}$ values fall well within the 1 σ range established in Figure 6.

5.3. *Spectral Energy Distribution: Parameter Grid Search*

Here we compare our synthetic SEDs to the absolute spectrophotometry of Vega. Specifically, we compare our models to the data-model composite SED[10] of Bohlin & Gilliland (2004), which includes *International Ultraviolet Explorer* (*IUE*) data from 125.5 to 167.5 nm, *Hubble Space Telescope* (*HST*) Space Telescope Imaging Spectrograph (STIS) data from 167.5 to 420 nm, and a specifically constructed Kurucz model shortward of *IUE* and longward 420 nm to match and replace data corrupted by CCD fringing in this wavelength region. To facilitate this comparison, first the synthetic spectra were convolved to the spectral resolution of the observations ($\lambda/\Delta\lambda = 500$), and then both the data and convolved synthetic spectra were binned: 2.0 nm wide bins in the UV (127.5–327.5 nm, 101 bins) and 2.0 nm bins in the optical and near-IR (330.0–1008 nm, 340 bins) for a total of 441 spectral bins.

[10] At ftp://ftp.stsci.edu/cdbs/cdbs2/calspec/alpha_lyr_stis_002.fits.

Figure 7 shows the χ_ν^2 map in the (ω, $T_{\rm eff}^{\rm pole}$)-plane. These two parameters, apart from the angular diameter, most sensitively affect the fit to the observed SED. There is a clear positive correlation between ω and $T_{\rm eff}^{\rm pole}$. This makes sense if one considers that a more rapidly rotating star will be more gravity darkened and require a hotter pole to compensate for a cooler equator in order to match the same SED. Following this correlation, it is expected that a continuum of models from ($\omega = 0.89$, $T_{\rm eff}^{\rm pole} = 10,150$ K) to ($\omega = 0$, $T_{\rm eff}^{\rm pole} = 9550$ K) will provide a reasonable fit to the SED since the nonrotating ATLAS12 model of Kurucz fits the observed SED quite well (Bohlin & Gilliland 2004). However, we did not consider models with $\omega < 0.88$ in the SED analysis because such models are a poor match to the CHARA/FLUOR squared visibility data set as shown above. In other words, although the ATLAS12 model provides a good fit to the observed SED, it fails to predict the correct center-to-limb darkening for Vega.

The best-fit synthetic spectrum is shown in Figure 8. Considering the complexity of this synthetic SED relative to a single $T_{\rm eff}$ model, there is generally good agreement ($\pm 5\%$) between our best-fit model and the data longward of 300 nm, apart from larger mismatches at the Paschen and Balmer edges and in the Balmer lines. Longward of 140 nm, the model agrees with the observations to within $\pm 10\%$. At wavelengths below 140 nm, as measured by the *IUE*, the data are up to a factor of 2 lower than predicted. Our best fit yields $\chi_\nu^2 = 8.7$. The overprediction below 140 nm has only a small effect on the synthetic integrated flux between 127.5 and 1008 nm, 2.79×10^{-5} ergs cm^{-2} s^{-1}, which is within 1.2 σ of the value derived from an integration of the observed SED, $(2.748 \pm 0.036) \times 10^{-5}$ ergs cm^{-2} s^{-1}. The equatorial angular diameter derived from this SED fit, $\theta_{\rm equ} = 3.407$ mas, differs from the best fit to the CHARA/FLUOR data, $\theta_{\rm equ} = 3.329$ mas, by 2.4%, a value within the uncertainty of the absolute flux calibration.

6. DISCUSSION

The best-fit stellar parameters, based on the model fits to the CHARA/FLUOR data and archival spectrophotometry in § 5, are summarized in Table 2. As discussed in § 3, the effect of extended K'-band emission in the Vega system, if unaccounted for, is to increase the apparent angular diameter of Vega slightly, by $\sim 0.3\%$. Correcting for this effect via equation (1), the best-fit equatorial diameter is shifted systematically lower by 0.3% (0.01 mas) to the range 3.31 mas $< \theta_{\rm equ} <$ 3.33 mas. We find that all other parameters in Table 2 are uneffected by the extended emission within the error bars given. The best-fit range for the fraction of the angular break-up rate, $0.89 < \omega < 0.92$, sensitive to

TABLE 2
FUNDAMENTAL STELLAR PARAMETERS FOR VEGA

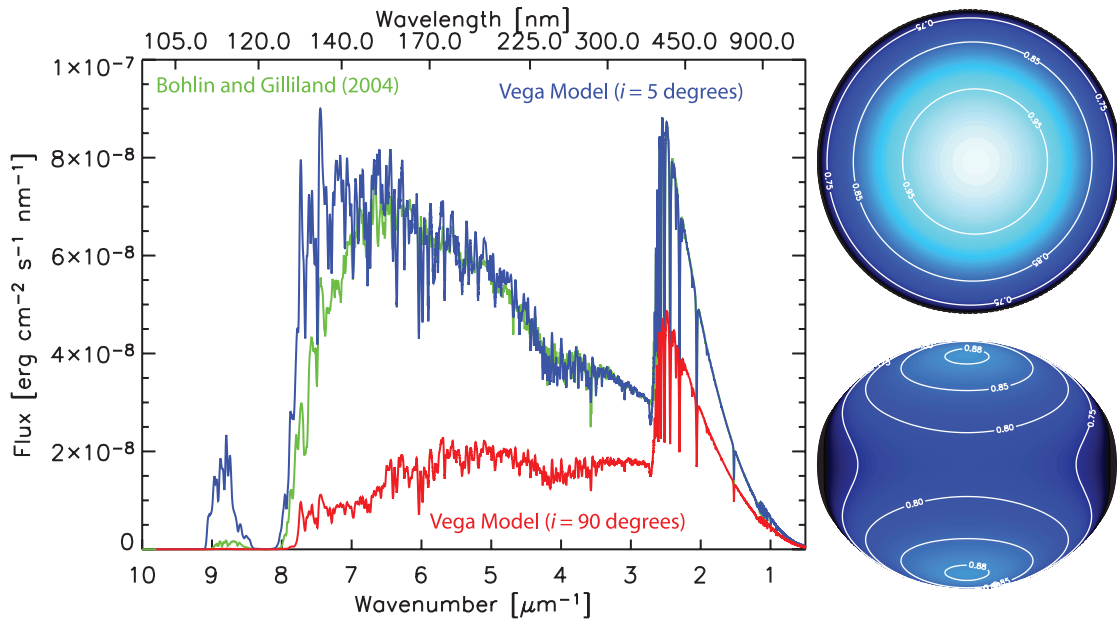| Parameter	Symbol	Value	Reference
Fraction of the angular break-up rate.........................	ω	0.91 ± 0.03	CHARA/FLUOR V^2 fit
Equatorial angular diameter (mas)	$\theta_{\rm equ}$	3.33 ± 0.01	CHARA/FLUOR V^2 fit
Parallax (mas)	$\pi_{\rm hip}$	128.93 ± 0.55	Perryman et al. (1997)
Equatorial radius ($R_\odot$)	$R_{\rm equ}$	2.78 ± 0.02	Eq. (2)
Polar radius ($R_\odot$)...	$R_{\rm pole}$	2.26 ± 0.07	Eq. (3)
Pole-to-equator $T_{\rm eff}$ difference (K)	$\Delta T_{\rm eff}$	2250^{+400}_{-300}	Eq. (8)
Polar effective temperature (K).................................	$T_{\rm eff}^{\rm pole}$	$10,150 \pm 100$	Fit to spectrophotometry (Bohlin & Gilliland 2004)
Luminosity ($L_\odot$)..	L	37 ± 3	Eq. (5)
Mass ($M_\odot$)..	M	2.3 ± 0.2	$(L/L_\odot) = (M/M_\odot)^{4.27 \pm 0.20}$ (from Sirius)
Polar surface gravity (cm s^{-2}).................................	$\log (g)_{\rm pole}$	4.1 ± 0.1	Eq. (4)
Equatorial rotation velocity (km s^{-1})	$V_{\rm equ}$	270 ± 15	Eqs. (13) and (15)
Projected rotation velocity (km s^{-1})........................	$v \sin i$	21.9 ± 0.2	Hill et al. (2004)
Inclination of rotation axis (deg)...............................	i	4.7 ± 0.3	Eq. (14)

Fig. 9.—*Left*: Comparison between the SED from Bohlin & Gilliland (2004; *IUE* and *HST* observations supplemented by a slowly rotating model spectrum both below 127.5 nm and longward of 420 nm) and two rapidly rotating models for Vega's SED, one viewed from an inclination of 5° (nearly pole on) and one viewed from an inclination of 90° (equator on), from an integration of two intensity maps via eq. (24) for these inclinations. *Right*: Comparison of the best-fit brightness distributions for Vega with inclinations of 5° (*top*) and 90° (*bottom*). For the equator-on view, the poles appear 10% fainter than the pole-on view due to limb darkening.

the amplitude of the second lobe, is unaffected by the extended emission because the V^2 correction is quite small there, $\Delta V^2 < 0.0003$, relative to the first lobe, where the correction is up to 20 times larger.

One parameter that stands out is our large pole-to-equator effective temperature difference, $\Delta T_{\mathrm{eff}} = 2250^{+400}_{-300}$ K, relative to previous spectroscopic and spectrophotometric studies of Vega (Gulliver et al. 1994; Hill et al. 2004) for which ΔT_{eff} falls into the range 300 to 400 K. Our larger ΔT_{eff} yields a much cooler equatorial effective temperature, $T_{\mathrm{eff}}^{\mathrm{equ}} = 7900^{+500}_{-400}$ K, than most recently reported for Vega, 9330 K (Hill et al. 2004). The amplitude of the second-lobe visibility measurements as observed by CHARA/FLUOR is well fit by strong darkening toward the limb. In the context of the Roche–von Zeipel model, such darkening requires a large pole-to-equator T_{eff} gradient. Consequently, we predict that Vega's equator-on SED (that is, viewed as if $i = 90°$ and integrated over the visible stellar disk; see eq. [24]) has a significantly lower color temperature and overall lower flux, particularly in the midultraviolet where the flux is lower by a factor of 5, as shown in Figure 9. A debris disk, aligned with Vega's equatorial plane as suggested by our nearly pole-on model for the star and the recent observations of a circular disk in the mid-IR (Su et al. 2005), should see a significantly less luminous, cooler SED than we see from the Earth. In the literature to date, modeling of the heating, scattering, and emission of Vega's dusty debris disk has assumed an irradiating SED equal to the pole-on view of Vega (see, e.g., Absil et al. 2006; Su et al. 2005). Our synthetic photospheric equatorial spectrum for Vega is tabulated in Table 3. It should be interesting to investigate how our predicted equatorial spectrum used in such modeling will affect conclusions regarding the amount of dust and the grain-size distribution in the debris disk.

Several of Vega's fundamental stellar parameters (ΔT_{eff}, V_{equ}, i) we derive differ significantly from those derived by Gulliver et al. (1994) and Hill et al. (2004) from high-dispersion spectroscopy. Regarding ΔT_{eff}, both spectroscopic studies find $\omega \simeq 0.5$, while we find $\omega = 0.91 \pm 0.03$. These two ω-values, along with

the corresponding $T_{\mathrm{eff}}^{\mathrm{pole}}$ values, 9680 and 10,150 K, in equation (8), yield ΔT_{eff} values of 350 and 2250 K. The reason the ω-values differ is at least partly linked to inconsistent parameters used in the spectroscopic studies. As noted in Hill et al. (2004), the Gulliver et al. (1994) study finds a low value for the polar gravity, $\log(g)_{\mathrm{pole}} = 3.75$, which yields a mass for Vega of only 1.34 $M_{\odot}$ and an inclination inconsistent with the expected equatorial velocity. The equatorial velocity of Hill et al. (2004), $V_{\mathrm{equ}} = 160$ km s^{-1}, is not consistent with their other parameters [$\omega = 0.47$, $\log(g)_{\mathrm{pole}} = 4.0$, $R_{\mathrm{equ}} = 2.73\, R_{\odot}$, $i = 7°.9$] which should yield instead $V_{\mathrm{equ}} = 113$ km s^{-1} and $i = 11°.1$. Values of $V_{\mathrm{equ}} = 160$ km s^{-1} and $i = 7°.9$ are recovered if $\omega = 0.65$, which corresponds to $V_{\mathrm{equ}}/V_{\mathrm{crit}} = 0.47$. It is possible to confuse ω with $V_{\mathrm{equ}}/V_{\mathrm{crit}}$. The two are not equivalent:

$$\omega = \frac{\Omega}{\Omega_{\mathrm{crit}}} \frac{V_{\mathrm{equ}}}{V_{\mathrm{crit}}} = 2 \cos\left[\frac{\pi + \cos^{-1}(\omega)}{3}\right]. \qquad (25)$$

TABLE 3
A Model Equatorial Photospheric Spectral Energy Distribution
for Vega from 1020.5 Å to 40 μm ($R = 500$)

Wavelength (Å) (1)	Flux $(F_{\lambda})^{\mathrm{a}}$ (ergs cm^{-2} s^{-1} Å^{-1}) (2)
1.020500000000000E+03	1.68027E+03
1.021000000000000E+03	1.65680E+03
1.021500000000000E+03	1.62296E+03
1.022000000000000E+03	1.57629E+03
1.022500000000000E+03	1.51370E+03

Note.—Table 3 is published in its entirety in the electronic edition of the *Astrophysical Journal*. A portion is shown here for guidance regarding its form and content.

[a] The flux at a distance d from Vega *in the equatorial plane* is the flux from col. (2) multiplied by the ratio $(R_{\mathrm{equ}}/d)^2$, the ratio squared of Vega's equatorial radius to the distance, or $(2.78/d)^2$ when d has the units of solar radii.

For $\omega = 0.65$, the corresponding $\Delta T_{\rm eff} = 757$ K, not 350 K. Therefore, there appears to be a mismatch between the $V_{\rm equ}$ and $\Delta T_{\rm eff}$ values used in the most recent spectral analyses, and this suggests the spectral data must be reanalyzed with a consistent model. A. Gulliver (2006, private communication) confirms that Hill et al. (2004) did confuse ω with $V_{\rm equ}/V_{\rm crit}$, and this group is now reanalyzing Vega's high-dispersion spectrum. Our best-fit value for ω, derived from the interferometric data, is appealing because, together with our derived polar effective temperature, it yields a luminosity consistent with that of slowly rotating A0 V stars. A more slowly rotating model for Vega will have a warmer equator and an overall higher true luminosity too large for its mass. Therefore, it seems that less rapidly rotating models for Vega do not offer an explanation for the apparent overluminosity with respect to its spectral type.

Our best-fit model, while it provides self-consistent parameters within the Roche–von Zeipel context, has several discrepancies, most notably producing too much flux below 140 nm relative to the observed SED. The limitations of the LTE metal-line blanketing for modeling Vega in the ultraviolet have recently been explored by García-Gil et al. (2005). They find that in the UV the line opacity is generally systematically too large in LTE because the overionization in non-LTE is neglected. Our best model flux below 140 nm is already too large, so a fully non-LTE treatment is not expected to improve this discrepancy. The Wien tail of Vega's SED will be the most sensitive to the warmest colatitudes near the pole. In our strictly radiative von Zeipel model, SEDs with $T_{\rm eff}^{\rm pole} < 10{,}050$ K produce too much flux in the optical and near-IR, so simply lowering $T_{\rm eff}^{\rm pole}$ will not solve the problem; the temperature gradient must differ from the $T_{\rm eff} \propto g_{\rm eff}^{0.25}$ relation. The equatorial effective temperature we derive, 7900 K, may indicate that Vega's equatorial region is convective. If so, von Zeipel's purely radiative gravity darkening exponent, $\beta = 0.25$, will not be valid near the equator. A more complex model, in which the gravity darkening transitions from purely radiative near the pole to partially convective near the equator, may be the next approach to take. Such a temperature profile may allow for a cooler $T_{\rm eff}^{\rm pole}$, reducing the flux discrepancy below 140 nm, while still matching the observed optical and near-IR fluxes. Such a gradient must also improve the match to the Balmer and Paschen edges and the Balmer lines.

7. SUMMARY

We have demonstrated that a Roche–von Zeipel model atmosphere rotating at 91% $\pm$ 3% of the angular break-up rate provides a very good match to K'-band long-baseline interferometric observations of Vega. These observations sample the second lobe of Vega's visibility curve and indicate a limb-darkening correction 2.5 times larger than expected for a slowly rotating A0 V star. In the context of the purely radiative von Zeipel gravity darkening model, the second-lobe visibility measurements imply a $\sim$22% reduction in the effective temperature from pole to equator. The model predicts an equatorial velocity of 270 ± 15 km s^{-1}, which together with the measured $v \sin i$ yields an inclination of $i \simeq 5°$, confirming the pole-on model for Vega suggested by Gray (1988) to explain Vega's anomalous luminosity. Our model predicts a true luminosity for Vega of 37 ± 3 $L_{\odot}$, consistent with the mean luminosity of A0 V stars from $W({\rm H}\gamma)$-M_V calibration (Millward & Walker 1985). We predict that Vega's spectral energy distribution viewed from its equatorial plane is significantly cooler than viewed from its pole. This equatorial spectrum may significantly impact conclusions derived from models for Vega's debris disk that have employed Vega's observed polar-view spectral energy distribution, rather than the equatorial one, which seems more appropriate given our observations.

REFERENCES

Absil, O., et al. 2006, A&A, 452, 237
Aumann, H. H., et al. 1984, ApJ, 278, L23
Bohlin, R. C., & Gilliland, R. L. 2004, AJ, 127, 3508
Ciardi, D. R., van Belle, G. T., Akeson, R. L., Thompson, R. R., Lada, E. A., & Howell, S. B. 2001, ApJ, 559, 1147
Collins, G. W. 1963, ApJ, 138, 1134
———. 1964, ApJ, 139, 1401
———. 1966, ApJ, 146, 914
Collins, G. W., & Sonneborn, G. H. 1977, ApJS, 34, 41
Coudé du Foresto, V., Ridgway, S., & Mariotti, J.-M. 1997, A&AS, 121, 379
Coudé du Foresto, V., et al. 2003, Proc. SPIE, 4838, 280
Cranmer, S. R., & Owocki, S. P. 1995, ApJ, 440, 308
Davis, J., Tango, W. J., & Booth, A. J. 2000, MNRAS, 318, 387
Elste, G. H. 1992, ApJ, 384, 284
García-Gil, A., García López, R. J., Allende Prieto, C., & Hubeny, I. 2005, ApJ, 623, 460

Gray, R. O. 1985, JRASC, 79, 237
———. 1988, JRASC, 82, 336
Gulliver, A. F., Adelman, S. J., Cowley, C. R., & Fletcher, J. M. 1991, ApJ, 380, 223
Gulliver, A. F., Hill, G., & Adelman, S. J. 1994, ApJ, 429, L81
Hanbury Brown, R., Davis, J., Allen, L. R., & Rome, J. M. 1967, MNRAS, 137, 393
Hardorp, J., & Strittmatter, P. A. 1968, ApJ, 151, 1057
Hauschildt, P. H., Allard, F., Ferguson, J., Baron, E., & Alexander, D. R. 1999, ApJ, 525, 871
Hearnshaw, J. B. 1996, The Measurement of Starlight: Two Centuries of Astronomical Photometry (Cambridge: Cambridge Univ. Press)
Hill, G., Gulliver, A. F., & Adelman, S. J. 2004, in IAU Symp. 224, The A-Star Puzzle, ed. J. Zverko, J. Ziznovsky, S. J. Adelman, & W. W. Weiss (Cambridge: Cambridge Univ. Press), 35
Hughes, D. W. 2001, J. British Astron. Assoc., 111, 266

Kervella, P., Ségransan, D., & Coudé du Foresto, V. 2004, A&A, 425, 1161
Kervella, P., Thévenin, F., Morel, P., Bordé, P., & Di Folco, E. 2003, A&A, 408, 681
Maeder, A., & Peytremann, E. 1970, A&A, 7, 120
McAlister, H. A. 1985, in IAU Symp. 111, Calibration of Fundamental Stellar Quantities, ed. D. S. Hayes & A. G. D. Philip (Dordrecht: Reidel), 97
McAlister, H. A., et al. 2005, ApJ, 628, 439
Mérand, A., Bordé, P., & Coudé du Foresto, V. 2005a, A&A, 433, 1155
Mérand, A., et al. 2005b, A&A, 438, L9
Millward, C. G., & Walker, G. A. H. 1985, ApJS, 57, 63
Mozurkewich, D., et al. 2003, AJ, 126, 2502
Ohishi, N., Nordgren, T. E., & Hutter, D. J. 2004, ApJ, 612, 463
Perrin, G., & Ridgway, S. T. 2005, ApJ, 626, 1138
Perryman, M. A. C., et al. 1997, A&A, 323, L49

Peterson, D. M., et al. 2004, Proc. SPIE, 5491, 65
———. 2006, ApJ, 636, 1087
Petrie, R. M. 1964, Publ. Dom. Astrophys. Obs. Victoria, 12, 317
Press, W. H., Teukolsky, S. A., Vetterling, W. T., & Flannery, B. P., ed. 1992, Numerical Recipes in FORTRAN (2nd ed.; Cambridge: Cambridge Univ. Press)
Stroud, A. H., & Secrest, D. 1966, Gaussian Quadrature Formulas (Englewood Cliffs: Practice Hall)
Su, K. Y. L., et al. 2005, ApJ, 628, 487
ten Brummelaar, T. A., et al. 2005, ApJ, 628, 453
van Belle, G. T., et al. 2006, ApJ, 637, 494
van Hamme, W. 1993, AJ, 106, 2096
von Zeipel, H. 1924a, MNRAS, 84, 665
———. 1924b, MNRAS, 84, 684

Note added in proof.—New closure phase operations of Vega at visual wavelenghts with the Navy Prototype Optical Interferometer (D. M. Peterson et al., Nature, 440, 896 [2006]) are also consistent with a rapidly rotating model for Vega. The Peterson et al. model establishes values for Vega's mass, equatorial velocity, polar surface gravity, inclination, angular velocity, polar radius, and equatorial effective temperature that overlap with our values within the uncertainties. While both the Peterson et al. model and our model appear to have the same Roche–von Zeipel formalism, the two data sets and models yield significantly different equatorial radii: $R_{equ} = 2.78 \pm 0.02 \ R_\odot$ (CHARA/FLUOR) versus $2.873 \pm 0.026 \ R_\odot$ (NPOI). This difference is directly linked to a difference in the derived angular size of Vega's equator in two studies: $\theta_{equ} = 3.33 \pm 0.01$ mas (CHARA/FLUOR) versus 3.446 ± 0.031 mas (NPOI). We do not at present understand the reason for this dependency.